Comparison of AC-Superconducting Multi-Phase Symmetric-Winding Topologies for Wind Power Generators with PM Rotors

Dany Josué Tomé-Robles, *Member, IEEE*, Robert Nilssen, and Jonas Kristiansen Nøland, *Senior Member, IEEE*

***Abstract*—In this paper, an AC superconducting multi-phase symmetric-winding machine is designed for a wind power generator to improve its performance and reduce losses, where four handpicked topological designs were explored and compared. In particular, it is found that using high-phase order of unique phasors further improves the performance. The iron losses are reduced, and the rippling behavior is lowered due to the smoother airgap magnetic flux density. Furthermore, a higher least-common-multiple (LCM) is achieved due to a better slot-pole combination for fractional-slot concentrated windings without having space sub-harmonics. Nonetheless, it is shown that creating a smooth airgap magnetic flux density does not improve the AC hysteretic superconducting losses; thus, further research is needed using additional approaches. Moreover, it is found that the Meisner effect is present in the machine and is inversely proportional to the AC hysteretic superconducting losses. Finally, the work shows that a 13-phase AC-superconducting machine can achieve a theoretical limit approaching $101.70\,\mathrm{Nm/kg}$ for the torque-to-weight ratio, outperforming classic winding layouts.**

***Index Terms*—AC losses, fractional-slot concentrated windings, harmonics, iron losses, multi-phase symmetric windings, superconducting coils.**

I. Introduction

NOWADAYS, the electric sector is changing rapidly towards a more sustainable energy supply. In particular, the growth of offshore wind power generation has been driven towards bigger wind turbines. Thus, the challenge to create more compact and lightweight structures and machines have become a necessity for the industry.

One of the technologies that have been investigated to create compact generators in recent years is electrical machines (EMs) made with superconductors. Recently three projects have been developed to prove the feasibility of DC-based superconducting machines (SCMs), i.e., a superconducting field winding to enhance the magnetic loading of the machine. Those include INNWIND [1], Suprapower [2], and EcoSwing [3]. The latter has been successfully proved with a technology readiness level (TRL) equal to 7, achieving an airgap shear stress that doubles compared to a conventional permanent magnet generator (PMG) and a weight reduction of up to 24%. In addition, promising results have been reported emphasizing the reliability and robustness of the generator design [4]–[7].

Manuscript received August 6, 2021; revised January 24, 2022; revised May 7, 2022; accepted June 20, 2022. (*Corresponding author: Dany Josué Tomé-Robles.*)

Dany Josué Tomé-Robles is with the Department of Electrical engineering, Information Technology and Cybernetics, University of South-Eastern Norway (USN), Porsgrunn, 3918, Norway, (e-mail: Dany.Robles@usn.no).

Robert Nilssen and Jonas Kristiansen Nøland are with the Department of Electric Power Engineering, Norwegian University of Science and Technology (NTNU), Trondheim, 7034, Norway, (e-mail: robert.nilssen@ntnu.no; jonas.k.noland@ntnu.no).

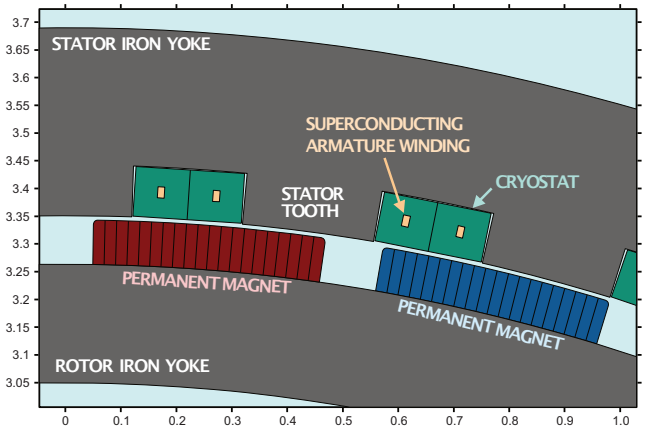

Fig. 1. Illustration of wind generator's machine geometry considered in the paper with slots designed according to cryostat requirements.

Further development of fully-superconducting solutions has been achieved for low-speed machines, in which the low frequencies cause the AC losses to decrease. Moreover, it is shown that one strategy to minimize total AC loss is by increasing the airgap flux density as a result of reducing the armature current needs, which also provides a safety margin to avoid quenching [8]. However, fully-superconducting generators require a rotating cryostat, making them more challenging to manufacture.

Permanent magnet (PM) excited AC-superconducting wind power generators do not have moving cryostat. However, the main issue is the demagnetization of the PMs, which is strongly related to the interaction with the stator slot design. It is also influenced by the PM dimensions and the current applied through the superconducting (SC) coils, which is the source of the magnetomotive force (MMF) for demagnetization. In order to avoid the demagnetization of the PMs, the MMF produced by the SC coil has to be restricted. Moreover, the airgap flux density is targeted to be $B_\delta \geq 0.25\,\mathrm{T}$ [9]. It has also been proved that an iron-cored, both stator and rotor, has better output torque capability and higher efficiency, compared to an iron-cored rotor air-cored stator [9]. In addition, slotted machines give better support to the coils, higher main flux and save SC material. Fig. 1 depicts an example topology, which will be further explored herein.

Another remarkable technology to further improve the performance and compactness of superconducting EMs is multiphase electrical machines (MEMs), which have been slightly assessed in prior studies. Nonetheless, the primary research focus has been on asymmetric windings, which have multiple sets of m-phase windings, letting aside the symmetric windings of high-phase orders. The main difference in having symmetric windings is that they are electromagnetically coupled with all the phases. In contrast, multiple asymmetrical sets of windings are magnetically coupled and electrically isolated in [10]. Furthermore, related to power electronics, symmetric multi-phase windings require control of only one electrical system, while asymmetric ones must control multiple electrical systems. The most common multi-phase control systems investigated are the prime-phase order topologies, e.g., 5-phase, 7-phase, and 11-phase windings. It is claimed that by adding more phases, the degrees of freedom in the control increases, e.g., for a 5-phase winding layout, a third harmonic in the dq-system can be controlled (d_3 and q_3) [11]–[20]. The power electronics scheme and control is not part of the scope of this paper, but there is supplementary information to the work carried out in this paper [21]. A higher number of phases can produce a more sinusoidal magnetic field than a machine with fewer phases, even if it has a similar number of slots. Moreover, "saturation harmonics", that travels at the same speed as the working harmonic, contributes to extra torque due to the airgap's flux distribution being flattened, avoiding the iron saturation and achieving a wider operational range. In summary, a MEM topology improves the torque density, decreases the cogging torque, lowers the ripple, reduces the rotor losses, and is more fault-tolerant [22]–[25].

This paper performs an investigation into AC-superconducting multi-phase symmetric-winding topologies for wind power generators with PM rotors to achieve compactness and feasibility. The usage of PM machines contributes to two utmost questions. 1) The performance of multi-phase superconducting PM machines; and 2) he analysis of the effects of the multi-phase system's smoother magnetic flux density into the AC armature superconducting coils. In addition, the demagnetization analysis should be covered in a future research effort. Our in-depth study is provided in the finite element analysis (FEA) environment, where the A-formulation is used [26] because it is already built in the COMSOL's physics. In future research, T- and H-formulations could be employed for deeper analysis [27].

The present paper is divided into the following six sections. Section II discusses the multiphase winding layouts and the design theory of high-phase order symmetric windings. Moreover, four windings layouts are taken as case designs and compared to assess the multiphase windings. Section III addresses the SCMs, their theory, and their superconductivity behaviour's formulation. In Section IV, the main analysis and the results are presented. Finally, section V provides critical discussions on the validity of the results before the paper is concluded in Section VI.

II. Multiphase winding layouts

A double-layer fractional-slot concentrated-winding (DL-FSCW) has been conveniently selected to reduce the use of SC material, while this winding topology also makes it easier to make a fair comparison of the various multiphase layouts. This is because an integer-slot winding layout requires different arrangements of poles. Hence, different topologies are needed to make the comparison, as presented in [21]. The larger the number of phases, the smaller the number of poles, which means lower electrical frequencies and more SC material. It is also worth mentioning that a stator with many slots is not possible because of the bending constraints of the SC armature coils, which further makes a case for the chosen DL-FSCW. For the winding layout design of m-phase fractional slot windings, it is essential to comply with specific conditions. First, quantity q_s, which is the number of slots per pole and phase, has to be reduced so that it's numerator and the denominator are the smallest possible integers, given by

$$q_s = \frac{Q_s}{pm} = \frac{z}{b}, \tag{1}$$

where Q_s is the total number of slots, p is the number of poles, and m is the number of phases.

A. Symmetry conditions

The three following conditions must be fulfilled to comply with a symmetrical winding for the DL-FSCW.

1) First symmetry condition: For double-layer windings, the first symmetry condition requires as follows.

$$\frac{Q_s}{m} = pq_s = p\frac{z}{b}, \quad \frac{p}{b} \in \mathbb{N} \tag{2}$$

2) Second symmetry condition: This condition is related to the divider t of Q_s and p. Which, in the end, can be written simply in the form; b and m cannot have a common divider, yielding

$$\frac{b}{m} \notin \mathbb{N}. \tag{3}$$

3) Third symmetry condition: For instance, a 24-phase winding, with $Q_s = 48$ and $p = 40$, it follows that $q_s = {}^1\!/_{20}$ is obtained, complying with the first and second symmetry condition. However, it does not generate 24 symmetric phases. Thus, the third condition for symmetry is proposed as follows.

$$\frac{Q'_s}{m} \in \mathbb{N} \tag{4}$$

This condition states that the slots per phase in a base winding shall be an integer number to achieve a multiphase winding. The base winding is the smallest independent symmetrical section of a winding. Therefore, when a winding consists of several base windings, it is possible to connect these base windings in series and in parallel to form a complete winding. The current and voltage of each base winding are due to geometrical reasons always the same in terms of phase and magnitude [28]. The number of slots of a base winding is calculated from

$$Q'_s = \frac{Q_s}{t} = \frac{Q_s}{GCD(Q_s, p/2)}, \tag{5}$$

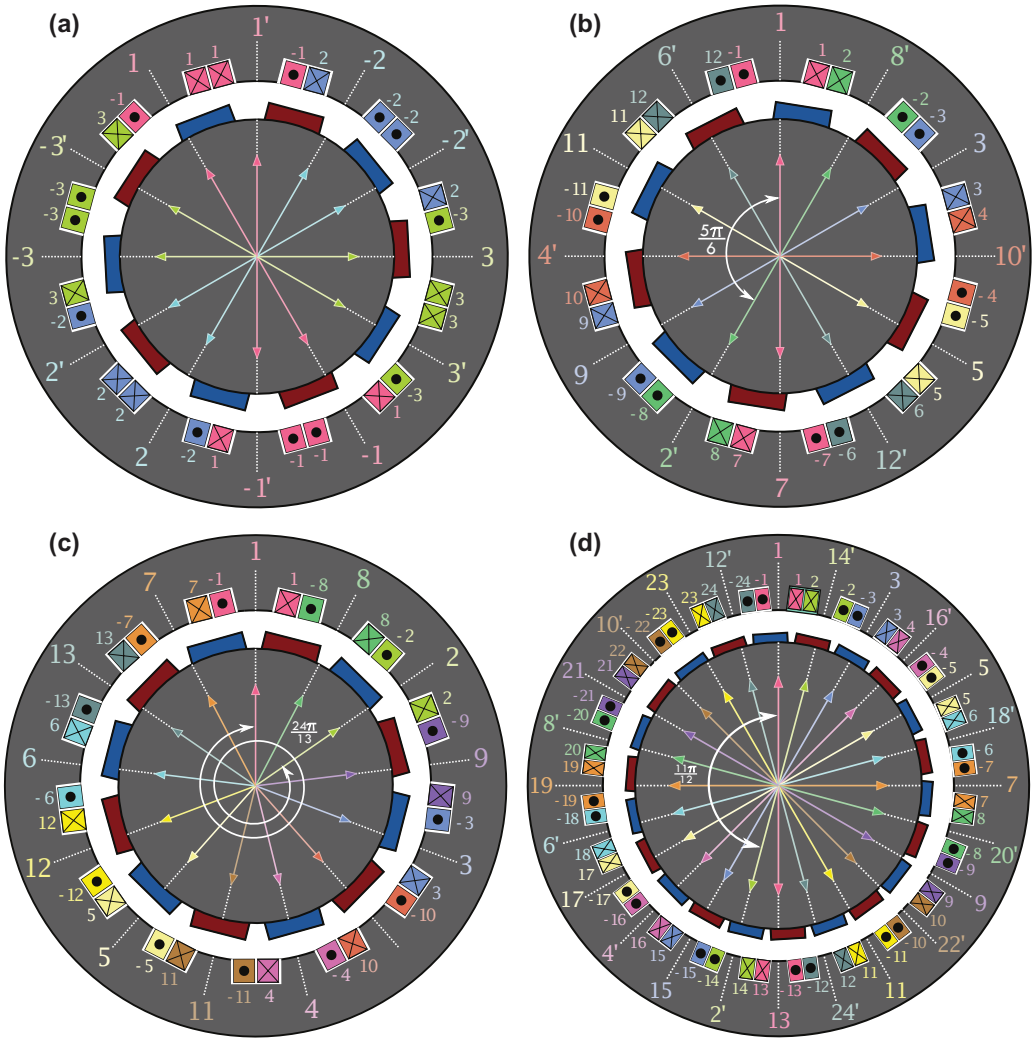

Fig. 2. Base winding topologies of different multiphase configurations. **(a)** 3-phase. **(b)** 12-phase (dual 6-phase). **(c)** 13-phase. **(d)** 24-phase (dual 12-phase).

where t is the number of independent winding sections. For instance, if a 9-phase machine wants to be constructed with a $Q_s = 48$ and $p = 40$, it is impossible because the number of slots per phase is fractional. Thus, a stator in which Q_s is not multiple of m, cannot be constructed. Hence, a slot-pole combination of $Q_s = 45$ and $p = 40$ will have one slot per phase, which gives a well designed multiphase machine. Furthermore, t is used to calculate the number of poles for a base winding, yielding

$$p' = \frac{p}{t} \tag{6}$$

B. Multiphase Winding Design

The reference machine considered in this paper, is taken from Dong Liu *et al.* [29], [30], to size the geometry accordingly for 15 MW. The generator has 48 slots and 40 poles. Using eqs. (5) and (6), the base winding for the reference three-phase machine is 12 slots, 10 poles, and $t = 4$, which is a quarter of the geometry. The multi-phase winding layouts are designed based upon the claim that more phases create extra torque contribution due to the flattened MMF [25]. Therefore, the multi-phase winding layouts are selected as follows.

1) 12-phase winding layout: This work aimed to perform a more straightforward comparison between topologies by having the same base winding as the three-phase winding layout, depicted in Fig. 2-(a). Therefore, by adopting the design philosophy of adding more phases to enhance the torque, it is found that the highest possible number of phases according to (4) is $m = 12$. Thus, a 12-phase winding layout is selected. Both winding layouts are shown in Fig. 2, subfigures (a) and (b). Thanks to having the same base winding, the comparison between them is more unambiguous, meaning that the only difference between the two geometries is how the coils are connected. Moreover, it is essential to notice that the topological layout has 12 coils as a symmetric winding design. However, the winding layout has only six unique phasors, resulting in a dual-six-phase machine, with redundant phases, yielding possibility for a fault-tolerant drive system design.

2) 24-phase winding layout: Following the emphasis on more phases to be equal to additional torque, a 24-phase winding is handpicked and designed to be compared with the findings of the 12-phase machine. Moreover, it also endorses the benefits of having double the number of phases with respect to the 12-phase machine. However, the symmetry

conditions do not comply if the geometry is kept unchanged. Thus, it is not possible to have the same base winding as a 12-phase and 3-phase machine according to (4), where $Q'_s/m = 12/24 = 1/2 \notin \mathbb{N}$. Therefore, a new base winding was constructed. The design philosophy, in this case, was to increase the number of poles from $p = 40$ to $p = 44$, obtained from eqs. (5) and (6). The base winding then becomes $Q'_s = 24$ and $p' = 22$, respectively, as shown in Fig. 2-(d). Then, the third symmetry condition complies with $Q'_s/m = 24/24 = 1 \in \mathbb{N}$. Nonetheless, the 24-phase symmetric winding layout has twelve unique phasors, resulting in a dual-twelve-phase machine, with even higher redundancy and more fault-tolerant design possibilities compared to the 12-phase machine.

3) 13-phase winding layout: Lastly, the researchers use another design philosophy of solely increasing the unique phasors as an objective. It was selected to show that it is the most intelligent way to design a symmetric multi-phase winding. Up to this point, the 24-phase machine had the highest number of unique phasors, equal to 12. However, by this design philosophy, it achieves a higher unique number of phasors, i.e., 13 unique phasors when a 13-phase winding layout is constructed. The slots and poles numbers are changed to $Q_s = 52$ and $p = 48$ respectively, to comply with the symmetry conditions, where $Q'_s/m = 13/13 = 1 \in \mathbb{N}$. The 13-phase winding layout is depicted in Fig. 2-(c).

C. Considerations on Alternative Multi-Phase Windings

The design philosophy's objective was to achieve the highest number of unique phasors while maintaining the minimum number of independent coils. The DL-FSCWs tend to make the third symmetry condition equal to 1. For instance, a 15-phase machine, with a similar geometry, will have $Q_s = 45$, $p = 48$ and $t = 3$, and a third symmetry condition equal to 1. Nonetheless, the maximum number of phases will depend on the physical constraints, e.g., stator's size, cooling system, and superconducting coils bending limits. For example, if the number of slots and poles is considered to be between 40 and 60, for a $15\,\mathrm{MW}$ slotted AC superconducting PM generator is physically feasible. The highest feasible unique number of phasors is 29, i.e., a prime number. Therefore, theoretically, a 29-phase machine with $Q_s = 58$ will have various slot-pole combinations that comply with the symmetry conditions. In theory, a 29-phase machine, with ripple reduction as the objective function, will be $Q_s = 58$, $p = 60$, $t = 2$, $LCM = 1740$ and $f = 3.78\,\mathrm{Hz}$. The base winding layout is half the geometry, with a working space harmonic of 15th order. Moreover, each power electronic module will be 518 kW to carry the power per phase. The controlling variables are embedded in a 29×29 square-matrix, where the controlled harmonics can be up to the 27th order according to [21]. More investigation into the design philosophy of multi-phase windings is needed, especially for double-layer fractional slot concentrated windings.

III. Superconducting coil

A superconductor's main characteristic properties are its high conductivity and the expelling of the magnetic field fluxes from the core material. These originate a zero DC resistance under specific conditions of 1) the temperature, 2) the critical current, 3) the magnetic field inside the material, and 4) its pressure. The latter property is particularly essential for room temperature superconductivity [31], while the others are important for low and high-temperature superconductivity $(4 - 77\ \mathrm{K})$.

TABLE I
Model Parameters for eqs. (7)-(9) representing the Superconducting Wire

Symbol	Quantity	Value
σ_c	critical conductivity	$4.38 \times 10^{12}\,\mathrm{S/m}$
E_c	critical electric field	$1 \times 10^{-4}\,\mathrm{V/m}$
J_c	critical engineering current density	$438.44\,\mathrm{A/mm^2}$
n	exponent factor[1]	25

[1] The exponent factor is handpicked to be in between $\mathrm{MgB_2}$ and REBCO typical values [33], [34].

The first three parameters presented in Table I must be within the critical range to avoid quenching of the superconductivity. The critical values depend on the SC material characteristics and the fabrication process. For use in EMs, the superconducting AC losses have to be reduced to obtain a good performance of the generator or motor. In particular, $\mathrm{MgB_2}$ is a good candidate due to low AC losses, and low price [32], [33]. However, this wire is produced with a cylindrical shape, which means that the magnetic field fluxes are isotropic around the whole material, yet this is true for one wire. For EM applications, the coils are constructed with several wires in which the penetration of magnetic field fluxes depends on the arrangements of the wire in the coil. Thus, the losses will depend on these topological arrangements. A high-temperature rectangular bulk superconductor wire is considered for model simplicity and computability purposes.

A typical superconductor wire is constructed with four layers arranged according to the geometry to improve stability, strength, and insulation, as shown in Fig. 4. Having these layers, four types of losses take place in the wire, e.g., 1) eddy current losses due to conducting layers; 2) coupling losses along with the metal layer between SC material filaments; 3) ferromagnetic losses that are the hysteresis losses of the metal itself; 4) C hysteresis losses due to varying fields. For the present paper, only the latter is considered. Moreover, we assumed the SC coil's operation temperature to be $65\,\mathrm{K}$.

The E-J power-law is used to formulate the superconductor's conductivity to properly model its interaction with the magnetic vector potential formulation in the COMSOL finite element analysis (FEA) environment (rotating magnetic machinery module). Moreover, in order to account for the non-bounder origin [35], [36], the following consideration is made.

$$J_c = \sigma_c E_c \tag{7}$$

$$|\mathbf{E}| = E_c \left(\frac{|\mathbf{J}|}{J_c} \right)^n \tag{8}$$

$$\sigma(|\mathbf{E}|) = \sigma_c \left| \frac{|\mathbf{E}| - E_c}{E_c} \right|^{1/n-1} \tag{9}$$

The parameters used in eqs. (7)-(9) are given in Table I.

In order to calculate the AC losses (P_{AC}), the SC material is assumed to be the entire geometry of the coil. The local current density variable $\mathbf{J}$ is computed as the engineering current density to account for the percentage of superconducting material in the whole wire. Thus, the losses are determined only by hysteresis behaviour by the following expression.

$$P_{AC} = \frac{1}{T}\int_{t_0}^{t_0+T}\left[\iint_S \mathbf{J}\cdot\mathbf{E}\,dS\right]dt, \tag{10}$$

The integration is taken over the conductor's cross-sectional area. To account for the transient phenomena, due to the bounded origin condition, the t_0 for the integration of (10) is postponed to the steady-state condition is reached. An existing superconductor model from [37]–[39] is used as reference geometry for this paper. The width and height are increased to be more manageable and achieve a higher critical current as shown in Fig. 4. The coil is modelled as a bulk superconductive surface with an engineering current density J_e (bulk SC engineering approach). The coil's geometry with its 15 turns (n_{coil}) is depicted in Fig. 4, where four parallel wires are incorporated in the total area of one turn to handle the rated current. With this new geometry, the following values are shown in Table II. All the machine's configurations are designed and simulated with 15 turns per coil and $4500\,\mathrm{A}$ as nominal current. The armature's coils are modelled radially aligned to construct the superconductor's racetrack easier.

The B-field's dependency on the critical current is not explicitly modeled in the E-J power law. Nonetheless, Fig. 3 shows the operation point at the constant engineering current density is at a load factor of $\sim$ 65%, according to load lines for the EUBCO $J_c - B$ characteristics. Also, a curve fitting is performed with the Kim model, i.e., (11), obtaining $J_{c0} = 1219\,\mathrm{A/mm^2}$ and $B_0 = 1.46\,\mathrm{T}$.

$$J_c = \frac{J_{c0}}{1 + \frac{|B_n|}{B_0}} \tag{11}$$

Therefore, the machines are operating within safe margins. Furthermore, Appendix B shows each topology's maximal and average applied perpendicular magnetic flux densities over time. The coefficients obtained could also be used to scale down the n-factor with respect to the magnetic field to make the modeling more accurate in high-field regions, were $n = \frac{n_{c0}}{1+\frac{|B_n|}{B_0}}$. However, more material data would be needed to make this type of modeling accurate, which could take more extreme magnetic field effects into account as well, especially in the edge regions of the SC coils.

IV. Topological Performance Analysis

The topologies are simulated with the specifications shown in Tables III, IV and V, with a machine geometry already depicted in Fig. 1 above. For a surface-mounted PM machine, the torque is as follows.

$$\tau = \frac{m}{4}\cdot p\cdot \Psi_m \cdot i_q \tag{12}$$

$$P = \frac{2}{p}\cdot\omega\cdot\tau \tag{13}$$

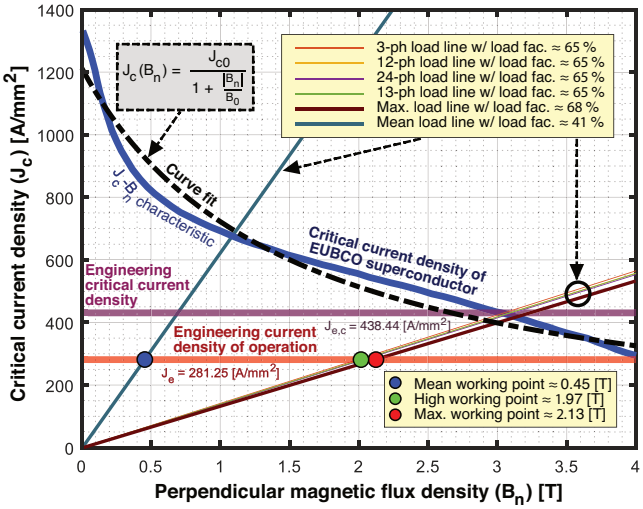

Fig. 3. $J_c - B_n$ Characteristic of EUBCO superconductor at 65 K. Material data adopted from [37] and curve fit expression taken from [40], with coefficient $B_0 = 1.465\,\mathrm{T}$ and $J_{c0} = 1219\,\mathrm{A/mm^2}$. The operation point and maximal operation point are obtained from Appendix B.

TABLE II
Key Geometrical Quantities and Electrical Characteristics of the Superconducting Wire

Symbol	Quantity	Value
h_{sc}	height of turn	$20.00\,\mathrm{mm}$
w_{sc}	width of turn	$0.80\,\mathrm{mm}$
A_{sc}	cross-sectional area of turn	$16.00\,\mathrm{mm^2}$
w_{coil}	coil width	$12.00\,\mathrm{mm}$
I_s	strand critical current	$219.22\,\mathrm{A}$
c_s	no. of parallel strands	8
I_c	wire critical current	$1753.76\,\mathrm{A}$
I_w	wire current	$1125.00\,\mathrm{A}$
i_w	normalised transport current (I_w/I_c)	0.64
c_w	no. of parallel wires[1]	4

[1] The number of parallel wires required to avoid superconducting quenching.

TABLE III
Rated Specification of the Handpicked Wind Power Generator

Symbol	Description	Value
P	electrical power[1]	$15.00\,\mathrm{MW}$
U	terminal voltage (rms)	$3300/\sqrt{3}\,\mathrm{V}$
I	phase current (rms)	$4500/\sqrt{2}\,\mathrm{A}$
S	apparent power	$18.19\,\mathrm{MVA}$
$\cos(\varphi)$	power factor	0.825
n	mechanical speed[2]	$72.19\,\mathrm{r/min}$
τ	mechanical torque	$18.95\,\mathrm{MNm}$
J_e	Engineering current density	$281.25\,\mathrm{A/mm^2}$

[1] A 15 MW machine is chosen because it is the biggest wind turbine reference model by the International Energy Agency (IEA) [41].
[2] The mechanical speed is obtained from the reference model.

Here, Ψ_m is the flux linkage of the magnet in the d-axis direction, and i_q is the current magnitude aligned in the q-axis. A maximum torque per ampere approach is targeted by aligning the current with the back-EMF voltage (i.e., q-current). This optimal angle is tracked to provide the basis for performing the dq0-transformation in the COMSOL Multiphysics numerical environment. The power factor and the reactance per unit are

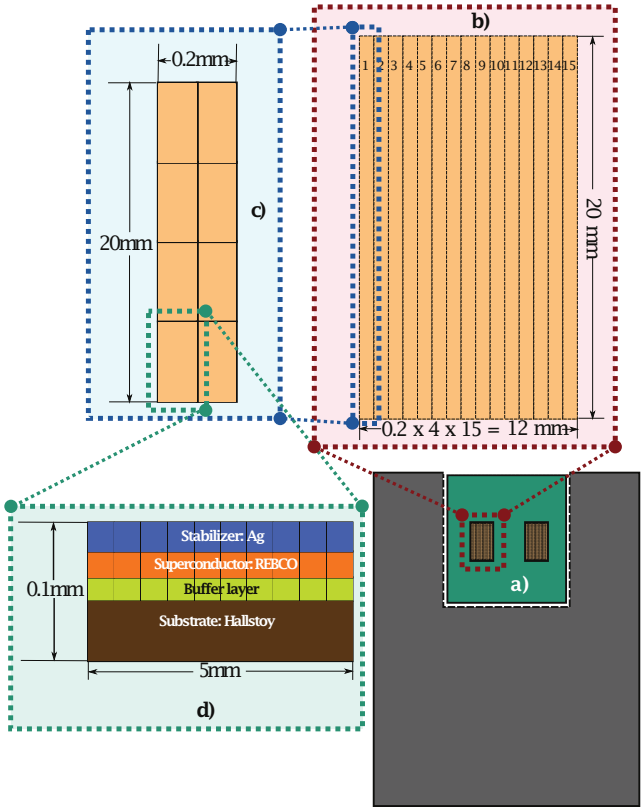

Fig. 4. a) SC coils tangentially arranged inside machine's slots, b) SC coil with its 15 turns, modelled as a bulk superconductive surface (I_r =4500 A), c) A resized SC wire that represent a quarter of one turn (I_c =1753.60 A), and d) SC real strand with its 4 layers for stability, strength and insulation (I_s =219.22 A).

TABLE IV
DESIGN SPECIFICATIONS OF THE HANDPICKED WIND POWER GENERATOR

Symbol	Description	Value
D_δ	airgap bore diameter	6693.80 mm
l_a	machine's active length	1506.10 mm
B_r	remanent magnet flux density	1.47 T
l_m	magnet's height	80 mm
α_m	magnet's coverage ratio	0.80
N_{coil}	number of turns per coil[1]	15
w_{cryo}	Cryostat's width	100 mm
h_{cryo}	Cryostat's height	92 mm

[1] The number of turns is obtained using the design equations. [42]

TABLE V
INVESTIGATED WINDING DESIGNS FOR THE WIND POWER GENERATOR

Symbol	Description	#3ph	#12ph	#13ph	#24ph
m	no. of phases	3	12	13	24
p	no. of poles	40	40	48	44
Q_s	no. of slots	48	48	52	48
t	no. windings sections	4	4	4	2
q_s	slots per pole & phase	$^2/_5$	$^1/_{10}$	$^1/_{12}$	$^1/_{22}$
N_{ph}	no. of turns per phase	240	60	60	30
k_{wdg}	Winding factor	0.9330	0.9659	0.9927	0.9914
LCM	$LCM(Q_s, p)$[1]	240	240	624	528

[1] The least common multiple between the number of slots and poles gives the cogging torque's empirical "goodness" value. The higher, the better. [43]

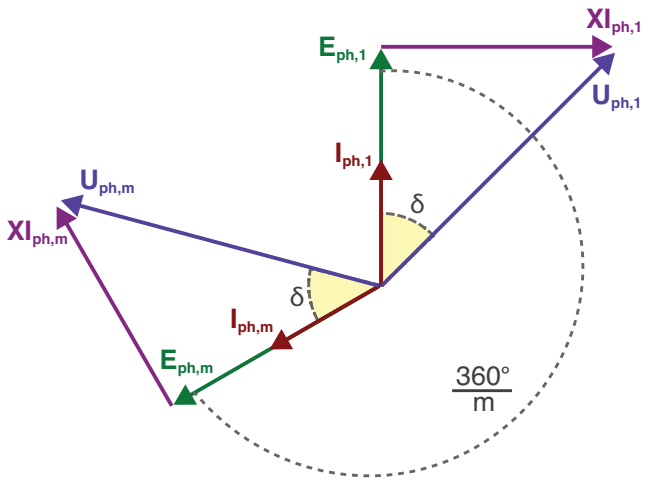

Fig. 5. Phasor diagram for m-phases with the current aligned in the q-axis.

calculated using the dq-transformed voltages.

Further, to determine the iron losses, the CAL2 method is employed [44]. For this approach, the α coefficient of the hysteresis loss density is set to 2, where the eddy current coefficient is replaced by a dynamic coefficient and the anomalous losses are not present due to the accuracy of the power coefficient of 1.5, whilst the hysteresis coefficient is kept as the Bertotti's model. The CAL2 method is expressed as follows:

$$p_{CAL2} = K_h(f,B)\cdot\hat{B}^2 f + K_d(f,B)\cdot\hat{B}^2 f^2 \tag{14}$$

According to [45], the third-order polynomial to fit K_h and K_d for a low-frequency range machine (e.g. $< 400Hz$) can be assumed to vary only in terms of the magnetic flux density $\hat{B}$. Thus the third-order polynomial curve fit for this work is described, yielding:

$$\begin{aligned} K_h(\hat{B}) &= k_{h0} + k_{h1}\hat{B} + k_{h2}\hat{B}^2 + k_{h3}\hat{B}^3, \\ K_d(\hat{B}) &= k_{d0} + k_{d1}\hat{B} + k_{d2}\hat{B}^2 + k_{d3}\hat{B}^3, \end{aligned} \tag{15}$$

where k_{hj} and k_{dj}, for $j = 0,1,2,3$, are constant to be determined by the curve fit. The constants are calculated by inserting these expressions into (14) and using the specific loss data for the iron core material in a curve-fitting tool. This is provided in Fig. 15 in the appendix. In order to compute the losses of the machine, the calculation has to be done in the time domain by time-stepping computations using FEA. In [46], the calculation of the loss density components are formulated as follows:

$$\begin{aligned} p_h &= \frac{1}{\pi T}\int_0^T K_h(f_1,\hat{B})\cdot B(t)\cdot\left[\frac{dB(t)}{dt}\right]\cdot dt \\ p_d &= \frac{1}{2\pi^2 T}\int_0^T K_d(f_1,\hat{B})\cdot\left[\frac{dB(t)}{dt}\right]^2\cdot dt \end{aligned} \tag{16}$$

TABLE VI
OBTAINED MEAN ELECTRICAL POWER OVER TIME

Topology	FEA	Analytical[1]	Deviation (%)
3ph machine	15.19 MW	15.94 MW	+4.72 %
12ph machine	15.79 MW	16.37 MW	+3.58 %
24ph machine	16.58 MW	17.45 MW	+4.99 %
13ph machine	17.41 MW	18.35 MW	+5.13 %

[1] Calculated from (13) and the values obtained of the flux linkage from table VII.

Furthermore, to compute the total component losses, volumetric integration is conducted, yielding:

$$P_h = \rho l_a N_{sector} \iint_S p_h \, dS, \qquad P_d = \rho l_a N_{sector} \iint_S p_d \, dS, \tag{17}$$

Where ρ is the density of the material, l_a is the active length of the machine, N_{sector} is the number of segments or sectors in which the entire machine is divided to be simulated in COMSOL, and S is the total integration area of the iron core of the machine.

A. Power, Shear Stress and Power Factor Analysis

The machine's power generation performance comparison is provided in Fig. 7. The rippling behaviour is even further reduced for the 13-phase machine than the 24-phase machine due to the unique phasors. Furthermore, fluctuating behaviour is observed in Arkkio's method used power calculation via the electrical torque. This action is due to the Meisner Effect of the superconducting armature coils, which is better highlighted in Fig. 6. Further, it shows that the 13-phase machine has the lowest average airgap magnetic flux density generated by the PMs, expecting the lowest power factor among all topologies. On the other hand, the output power for the 13-phase machine is increased because of the higher electrical frequency due to the 48 poles, as shown in Tables VI and VII.

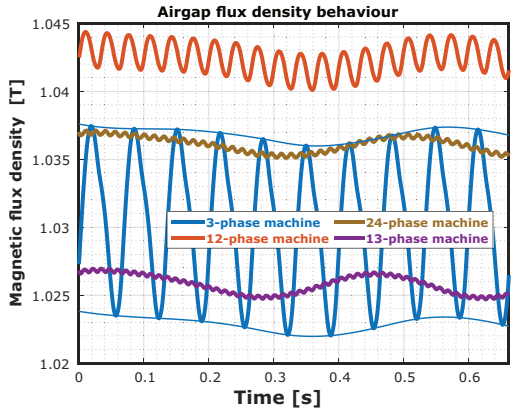

Fig. 6. Airgap magnetic flux density behaviour over time calculated inside the Arkkio's band.

According to Pyrhönen [28], the conventional shear stress for air-cooled machines is around 59.5 kPa, so at least to double that, the shear stress of an SCM should be around 120 kPa. For the present work, the calculated shear stresses

TABLE VII
OBTAINED FLUX LINKAGE AND RATED FREQUENCY

Topology	Flux linkage (FEA)	Electrical frequency
3ph machine	149.147 Wb	2.520 Hz
12ph machine	38.297 Wb	2.520 Hz
24ph machine	18.559 Wb	2.772 Hz
13ph machine	33.026 Wb	3.024 Hz

TABLE IX
OBTAINED POWER FACTOR AND MACHINE REACTANCE

Topology	Power factor[1](pf)	Reactance[2](x)	Reactance[3](x)
3ph machine	0.73	0.68 pu	0.66 pu
12ph machine	0.73	0.68 pu	0.68 pu
24ph machine	0.72	0.69 pu	0.74 pu
13ph machine	0.71	0.71 pu	0.73 pu

[1] Calculated with the dq voltages as follows: $V_q/\sqrt{V_d^2+V_q^2}$
[2] Calculated with the power factor as follows: $\sqrt{1-pf^2}$
[3] Calculated with the terminal voltage, Back-EMF and rated current as follows: $\sqrt{V_t^2-E_0^2}/I_{rated}$

surpass this criterion. In Table VIII, the shear stress values are presented, proven to be at least three times classical machines.

TABLE VIII
OBTAINED SHEAR STRESS FOR THE STUDIED SCM TOPOLOGIES

Topology	Shear stress	Increase
3ph machine	182.32 kPa	0.00 %
12ph machine	189.47 kPa	+3.92 %
24ph machine	199.12 kPa	+9.21 %
13ph machine	209.04 kPa	+14.66 %

Increasing the number of phases enhances the output power and further reduces rippling behaviour. For the 12-phase winding layout, the output power, compared to the 3-phase, is enhanced even though they share the same geometry and slot-pole combination. For the 24-phase and 13-phase winding layouts, the output power is further increased due to the increase of poles, which means higher electrical frequency.

Moreover, the cogging torque is further reduced with a multiphase fractional winding layout because the LCM is further increased. For the 3-phase and 12-phase winding layouts, the LCM is 240. For the 24-phase and 13-phase windings layouts, the LCMs are 528 and 624, respectively. Hence, the slot-pole combination can be further improved with multiphase FSCW whilst achieving a good winding layout design.

The power factor and reactance per unit are calculated for each model, as is shown in Table IX. Compared to the reference machine, the power factor is enhanced due to the higher remanent flux density used in the magnets. On the other hand, the power factor depends on the magnetic storage capability of the PM rotor. Two main phenomena are present for a high-phase order machine that reduces the magnetic storage capability of the magnets, resulting in a lower power factor: 1) a high armature reaction that demagnetizes more the PMs; 2) the reduction in the PMs volume by increasing the number of poles for the same machine's diameter.

B. Time and space Harmonics

The time harmonics are calculated at full-load for every winding layout, as is depicted in Fig. 8. It can be seen that

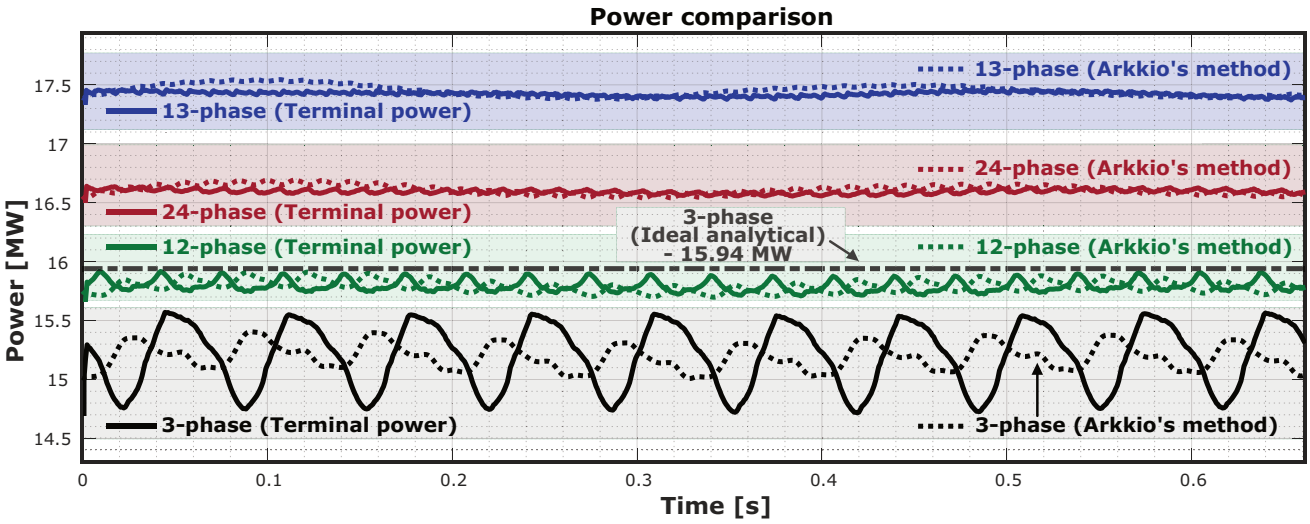

Fig. 7. Machine's power comparison with only q-axis current of $4500\,\mathrm{A}$ and mechanical speed of $72.2\,\mathrm{r/min}$. Arkkio's power are obtained from the Maxwell stress tensor, while the reference power calculation is made adding up the instantaneous AC power for all the phases. Straight line, obtained from (13) which gives a deviation of 4.73%.

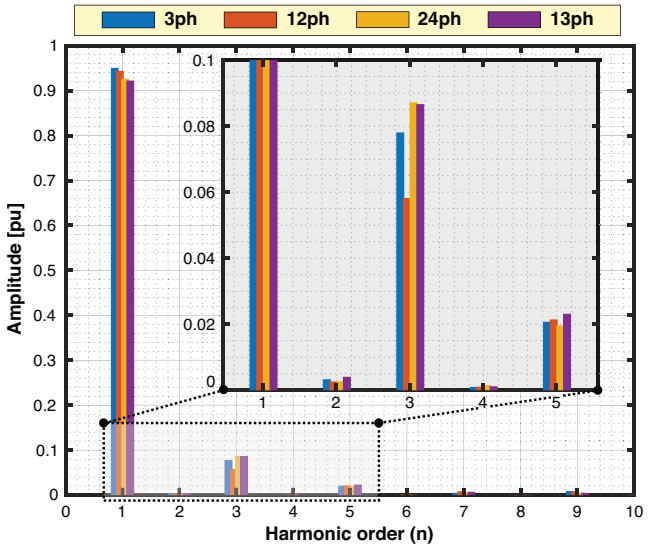

Fig. 8. Time harmonics comparison.

a 12-phase machine improves the performance by reducing the third-order harmonic compared to the 3-phase machine. However, the third-order harmonic marginally increase for the 24-phase and 13-phase machines, and the fundamental harmonics slightly decrease.

The space harmonics are calculated from the airgap radial magnetic flux density as is shown in Fig. 9. For spatial harmonics, the fundamental harmonic can be called working harmonic or main harmonic. Its harmonic order will depend on the slot-pole combination of the FSCW. The working harmonic is equal to the base pole-pairs of each winding layout. Because the 3-phase and 12-phase machines share the same geometry, they will have the same base pole-pairs $p'_r = 5$, which can be directly counted in Fig. 2. For the 24-phase topology, $p'_r = 11$, and for the 13-phase machine, $p'_r = 6$. The symmetric multi-phase winding layouts eliminate the space sub-harmonics

TABLE X
OBTAINED SPATIAL HARMONICS

Topology	Sub-harmonic value	Working Harmonic	
		Order	Value
3-phase	0.11	5	1
12-phase	0	5	1.02
24-phase	0	11	1
13-phase	0	6	0.98

without any heuristic algorithm or two or more different star-systems combinations for asymmetric or split-phase windings such as those presented in [47], [48]. The elimination of the space sub-harmonics, which rotates asynchronously with respect to the rotor, cancels the iron losses produced by large eddy currents, which explains why the 12-phase machine gives better performance than the 3-phase machine, even sharing the same geometry. Furthermore, the space working harmonic for the 13-phase winding layout is lower than the others, as shown in Table X. However, the machine's higher winding factor (as shown in Table V) and higher electrical frequency give a better output power. Nonetheless, a high space super-harmonic close to the working space harmonic could be further reduced with proper optimization for winding designs.

C. Iron Core Losses

The iron losses calculated with the CAL2 method are presented in Table XI. Furthermore, a relative percentage comparison is made between the models in Fig. 10, in which the 3-phase machine is taken as a reference, where the other topologies losses are re-computed relatively to the 3-phase machine to make a proper comparison. First, the iron losses are computed as a percentage of the total machine electrical power. This graph shows that the ripple reduction of high-phase order machines contributes to reducing iron losses. The advantages are clear to assess for the 12-phase machine, which has the same geometry as the 3-phase machine, shows a reduction of 14.35% in the relative iron losses. The 24-phase machine

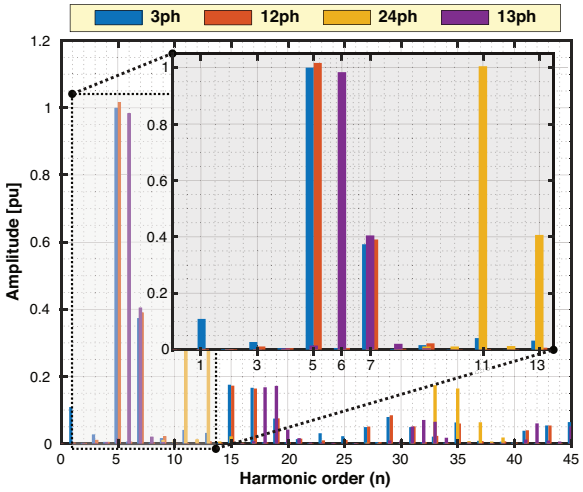

Fig. 9. Space harmonics comparison, where the three-phase machine is taken as the reference amplitude for normalization. The harmonic order is equal to the base pole-pair number $n = p'_r$ where $p'_r = 1, 2, 3, 4, 5...$ The working harmonic is the base pole-pair number for each topology, operating at a fundamental electrical angular frequency $\omega_e = 2\pi f$ according to Table VII, respectively. The mechanical angular frequency $\omega_m = 2\pi \frac{f}{t \cdot p'_r}$ is the same for all topologies.

TABLE XI
IRON LOSSES COMPARISON.

Model	Hysteresis losses	Dynamic losses	Total iron losses
3ph machine	36.41 kW	0.75 kW	37.15 kW
12ph machine	32.50 kW	0.57 kW	33.07 kW
24ph machine	35.70 kW	0.74 kW	36.43 kW
13ph machine	36.15 kW	0.85 kW	37.00 kW

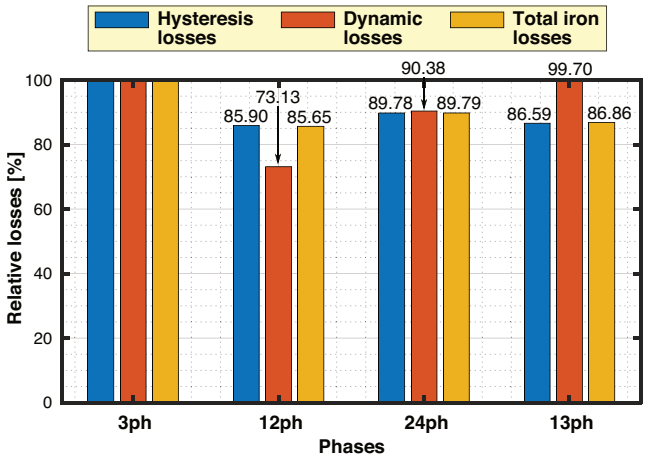

Fig. 10. Iron losses comparison relative to three phase topology.

reduces the percentage of iron losses compared to the 3-phase machine. However, due to iron saturation and frequency operation regime, the 24-phase is not improved further than the 12-phase case. The same happens to the 13-phase machine. Nonetheless, it is essential to remark that for the 13-phase machine, the power is increased by 14.66%, and the relative total iron losses are decreased 13.14% compared to the 3-phase machine.

TABLE XII
AC SUPERCONDUCTING LOSSES WITH OR WITHOUT LASER-SCRIBING TECHNIQUE

Model/Fabrication	Non-scribed	Scribed - 10 filaments
3ph machine	83.05 kW	8.30 kW
12ph machine	83.64 kW	8.36 kW
24ph machine	72.04 kW	7.20 kW
13ph machine	59.73 kW	5.97 kW

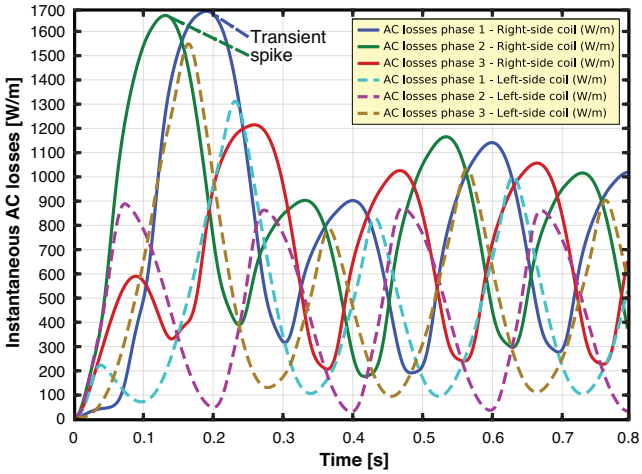

Fig. 11. Instantaneous AC losses for all the phases in a 3-phase machine. One coil side for each phase is shown to identify the different behaviour of the AC losses depending on the amount of magnetic flux density lines crossing the coil.

D. AC Superconducting Losses

The AC losses can be reduced per every filament scribed by laser-scribing fabrication techniques. E.g. the wire is scribed with ten filaments. Hence, the AC losses are reduced to a tenth of the non-scribed version. In Table XII, the AC losses are presented for all the models with the assumption of the laser scribing technique to reduce further the AC losses.

A good multiphase winding layout enhances the performance by reducing the iron losses and overall rippling behaviour. However, the smoothness of the magnetic flux densities in the airgap provided by high-phase order machines does not reduce the hysteresis AC superconducting losses because it depends mainly on the magnetic flux lines' tilt angle. Moreover, it is known that the stronger the armature reaction, the more tilted is the magnetic flux lines' angle, i.e., Maxwell Stress Tensor Analysis. Thus, the magnetic flux lines are assessed by computing the instantaneous AC losses for the 3-phase machine for one coil side of each phase to depict the AC losses depending on the coil's location inside the slot. For example, Fig. 11 shows that the right-side coils have more AC losses due to there being more magnetic flux lines, hence, higher magnetic flux density in that region of the slot, as is shown in Fig. 12.

Further, a manual parametric sweep of the coil's angular position is performed in steps of $5\,^\circ$ to find a local minimum of AC losses for the 12-phase machine, as is shown in Tables XIII and XIV. With a coil's angular position of $-35°$ for the right-side coil and $-20°$ for the left-side coil, the AC losses are reduced up to $4.5815\,\mathrm{kW}$ for ten filaments scribed.

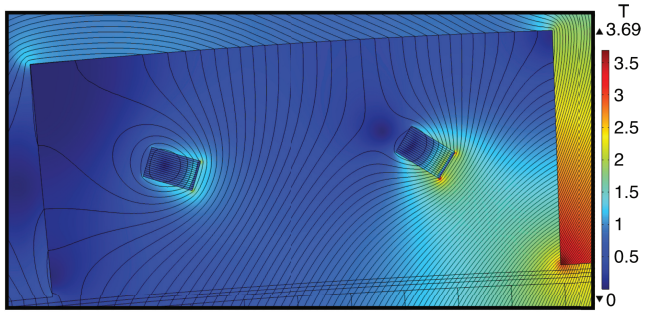

Fig. 12. Coils' angle optimization, where the left coils and right coil are at $-20\,^\circ$ and $-35\,^\circ$ measured from the horizontal axis, respectively. The time instant is handpicked at the end of the steady-state period T, which is one electrical period after the end of the transient period (t_0) of simulation.

TABLE XIII
AC LOSSES - COIL'S ANGLE DEPENDENCY

Coil angle	AC losses	Reduction
$0\,^\circ$	68.22 kW	0.00%
$-5\,^\circ$	63.34 kW	-7.15%
$-10\,^\circ$	59.36 kW	-12.99%
$-15\,^\circ$	55.27 kW	-18.99%
$-20\,^\circ$	51.78 kW	-24.09%
$-25\,^\circ$	49.61 kW	-27.28%
$-30\,^\circ$	47.62 kW	-30.20%
$-35\,^\circ$	46.44 kW	-31.93%
$-40\,^\circ$	46.83 kW	-31.36%
$-45\,^\circ$	47.40 kW	-30.52%

TABLE XIV
LEFT COIL ANGLE VARIATION

Left coil angle	Right coil angle	AC losses	Reduction
$-30\,^\circ$	$-35\,^\circ$	46.14 kW	-32.36%
$-25\,^\circ$	$-35\,^\circ$	46.00 kW	-32.57%
$-20\,^\circ$	$-35\,^\circ$	45.81 kW	-32.84%
$-15\,^\circ$	$-35\,^\circ$	46.00 kW	-32.58%

The angle is measured with respect to the horizontal axis, and the centre of the coils is the slot's centre, as shown in Fig. 12. Furthermore, it is seen that the flux lines enter more perpendicular to the coil's side. In Fig. 13 it can be seen that with a reduction in the AC losses, the fluctuating behaviour calculated with Arkkio's method increases, meaning the Meisner effect increases as well. Thus, perpendicular flux lines to the coil's side can decrease further the AC losses. However, this also creates more repulsion of the magnetic flux densities, i.e., Meisner effect, creating a stronger magnetic flux density fluctuation in the airgap, harming the machine's mechanical integrity.

Therefore, depending on the machine's loading, the magnetic angle is further tilted, changing the superconducting AC losses of the coils. Thus, a design philosophy for one angular position of the armature superconducting coils at full load or no-load is not a good design since the superconducting AC losses are very sensitive to the magnetic flux density angle inside the slot. One solution could be a new design of the slots. However, this complicates the design of the cryocooler. Hence, a 3D design of the superconducting armature coils can solve the angle sensitivity by arranging twisted or non-planar coils inside the racetrack.

E. Efficiency and Torque Density

The overall efficiency is calculated as follows.

$$\eta = \frac{P_{out}}{P_{out} + P_{loss,AC} + P_{cryo} + P_{Fe}} \times 100\% \tag{18}$$

Here, P_{out}, $P_{loss,AC}$, P_{cryo} and P_{Fe} are output power, AC losses in armature windings, cryocooler power, and iron loss respectively. Moreover, the cryocooler power is calculated by:

$$P_{cryo} = \frac{1}{\eta_{cryo}} \cdot \frac{T_{amb} - T_{cryo}}{T_{cryo}} \cdot P_{loss,AC} \tag{19}$$

Where T_{amb}, T_{cryo} and η_{cryo} are the ambient temperature, cryocooler temperature and cryocooler efficiency, respectively. The ambient temperature is set to $T_{amb} = 300\,\mathrm{K}$, the cryocooler temperature to $T_{cryo} = 65\,\mathrm{K}$, and the cryocooler efficiency is handpicked to be $\eta_{cryo} = 22\%$, being inside the physical range according to [38], [49], [50].

TABLE XV
CALCULATED EFFICIENCY

Topology	Efficiency (η)
3ph machine	98.82%
12ph machine	98.88%
24ph machine	99.03%
13ph machine	99.20%

It is shown in Table XV that the 13-phase machine has higher efficiency than the other topologies. Furthermore, in Table XVI, the highest torque-to-weight (TTW) is for the 13-phase machine. In comparison to the work done by Sung et al., [51] showcases an HTS field winding for a wind power generator that has a TTW of $137.38\,\mathrm{Nm/kg}$ for the active weight. For the present paper, the TTW for the 3-phase machine is $137.83\,\mathrm{Nm/kg}$ (i.e., only active mass), which verifies the design's effectiveness. In the end, the 13-phase machine with TTW of $184.9122\,\mathrm{Nm/kg}$ increases by 34% the torque density, which means that it has the highest torque density.

V. DISCUSSION

There are some reservations regarding the results presented in this paper. In reality, the design philosophy of a slotted AC-superconducting PM generator must consider the electric and magnetic loading to limit the demagnetization, e.g., it could cause a reduction in the remanent flux density of the magnets that could worsen the power factor. Therefore, the machine's compactness could be compromised due to a too high current loading, creating a significant armature reaction that reduces the magnetic loading. In the opposite direction, reducing the electric loading while keeping the nominal power increases the size of the machine. A reference model was utilized to resize the machines presented in this research paper, employing the design philosophy of making the airgap magnetic loading kept at 1 T.

Alternatively, the design philosophy for a fully-superconducting machine follows a different path. Since the SC properties dominate the electric and magnetic loading, these can be increased far more than a slotted

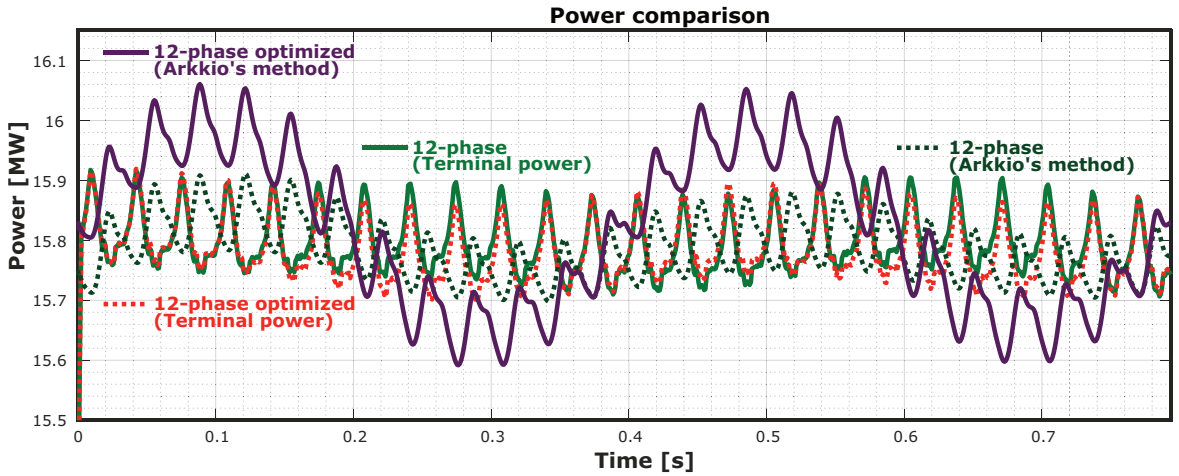

Fig. 13. Power comparison of the 12-phase and optimized version. It is depicted with Arkkio's method calculation that the Meisner effect increases when the AC losses are reduced, i.e. more magnetic field repulsion.

TABLE XVI
TORQUE-TO-WEIGHT (TTW) COMPARISON FOR THE FOUR HANDPICKED MULTIPHASE TOPOLOGIES

Parameter	3ph	12ph	24ph	13ph
W_{iron}	124.10 ton	124.10 ton	113.89 ton	103.85 ton
W_{SC}[1]	284.20 kg	284.20 kg	284.20 kg	307.88 kg
W_{mag}[2]	14.79 ton	14.79 ton	14.79 ton	14.79 ton
W_{total}[3]	139.18 ton	139.18 ton	114.19 ton	118.95 ton
TTW_{active}[4]	137.83 Nm/kg	143.27 Nm/kg	183.45 Nm/kg	184.91 Nm/kg
TTW_{Total}[5]	75.81 Nm/kg	78.80 Nm/kg	100.90 Nm/kg	101.70 Nm/kg

[1] The weight density of the REBCO superconducting tape is $8.19\,\mathrm{g/cm^3}$ according to [37].
[2] The neodymium magnet density is set to $7.40\,\mathrm{g/cm^3}$.
[3] Active weight of the machine.
[4] The Torque-To-Weigth is calculated with FEA values from table VII and (13).
[5] TTW calculated by assuming a non-active mass of 55% of the total machine's weight.

AC-superconducting PM generator. On the one hand, a fully-superconducting machine can be super-compact. On the other hand, the cooling systems become far more complex, and the iron flux paths tend to be highly saturated. Hence, ironless topologies are a common option for fully-superconducting machines. However, it demands more SC materials to create higher electric and magnetic loading. Thus, shielding is needed to reduce the influence of the high magnetic field. In the end, the technology readiness of the machine is unmatured, and the prices are high.

For this reason, selecting a slotted AC-superconducting PM generator reduces the cooling system complexity since the SC coils are in the stator, and the iron flux paths are less saturated. Additionally, a slotted topology reduces the influence of the magnetic field over the SC coils, and the technology readiness of PMs is mature.

Therefore, when comparing the AC losses between the present models and the reference model in [38], i.e., 31.7 kW; lower AC losses are computed since the magnetic loading decreases, and the iron flux paths reduce the magnetic field interaction with the SC coils. Then, the topologies must be similar to have a proper comparison, e.g., slotted AC superconducting PM machines. Hence, to validate the AC losses, a comparison is made with reference [52], which reports a 10-MW AC superconducting PM wind power turbine with AC losses equal to 5.57 kW, around 67% less than the present model. Nevertheless, the output power is approximately 67% less than the present models. Moreover, the compactness ratio regarding the machine's length is 63%. Hence, there is consistency in the AC losses value because both machines have the same design philosophy and topology, i.e., slotted AC superconducting PM generator.

Additionally, it is stated in [26] that a constant current density and an n-factor lead to overestimating the AC loss at B-fields above the full penetration. Nonetheless, the AC losses results give lower values than the reference model. Moreover, in references [32], [53] conclude that for frequencies below 10 Hz, the impact of the non-superconducting layers is not relevant to the model.

Moreover, the rationale behind the load factor equal to $\sim$ 65% relies on the following key assumptions.

1) A bulk SC engineering approach is used to scale up the geometry of the SC by applying the engineering current density (J_e).
2) The bulk geometry is set to be rectangular. The number of SC strands should be an even number assuming all strands have the same size.
3) The given even number of SC strands causes big jumps between feasible geometries, and normalized current values.
4) The dimensions of the strands are based on a reference model (i.e., a commercially obtainable strand), meaning

that the strand's specification limits the overall size of SC coils.

Furthermore, it is possible to change the number of parallel SC strands from 8 to 6 and obtain a normalized current of $\sim 85\%$. However, this value is considered to have a too-small safety margin. Therefore, further work should focus on optimizing the number of parallel strands, as already done in aerospace applications [54]. Moreover, a reconsideration of the stacking of SC layers should be done to reduce further the AC losses according to [55]. Additionally, since the reference machine is taken from [29], [30], the terminal voltage is fixed to a specific value, giving the total current and the number of turns per phase. Future work may reconsider the voltage value and number of turns per phase to optimize the superconducting material.

Finally, a short-circuit analysis should be performed, since the short-circuit current may be approximated as $I_{sc} \approx \frac{4500A}{0.66} = 6818.18\,\mathrm{A}$ (based on a phase reactance value of $0.66\,\mathrm{pu}$), which gives a normalized phase current (rms) around; $I_{sc} \approx \frac{6818.18A}{7015.04A} = 0.9719\,\mathrm{pu}$. Hence, the actual safety margin may comply with a sudden three-phase short circuit. Moreover, according to Liu et al. in [30], it is very likely a quench of superconductivity due to a three-phase short circuit for $\mathrm{MgB_2}$.

A better E-J power-law formulation with B-field dependency will improve the AC losses accuracy. Moreover, as is shown in Fig. 14, the outer areas of the coils have a higher current density distribution, and in Appendix B, Fig. 18 shows that in the inner coil turns, the maximal applied perpendicular magnetic field is reduced. The majority of the SC material operates under far lower magnetic flux densities as the mean values are around $0.45\,\mathrm{T}$. Moreover, if one considers iron sheaths or shielding to the external coil's turns could further improve the performance, reducing the peak magnetic fields. It can be seen that after one cycle, the maximal applied perpendicular magnetic field is decreased. Thus, a further investigation only for steady-state is needed. However, following the paper's scope, it is shown that the AC losses can be reduced by a proper angular position of the SC coils inside the slots. Furthermore, a critical phenomenon that affects the machine's integrity is observed when the torque ripple is reduced, the Meisner effect of the rotating magnetic field over the SC coils.

Finally, the multi-phase winding design could improve the harmonics if a four-layer or multi-layer FSCW is considered to perform a short-pitched winding design. For example, in [56]–[58], a multi-layer design shows a further reduction in the overall rotor losses, unbalanced magnetic pull, and torque ripple. On the other hand, for the present calculation, the current is purely sinusoidal; thence, a harmonic injection control system may reduce the losses and improve the overall performance of the machines [12], [13], [15], [25], [59]–[64]. Moreover, the number of phases can be considered according to the number of parallel- and series-connected converters [65].

VI. Conclusions

The present work analyses slotted AC superconducting machines (SCMs) with multiphase topologies and PM rotors.

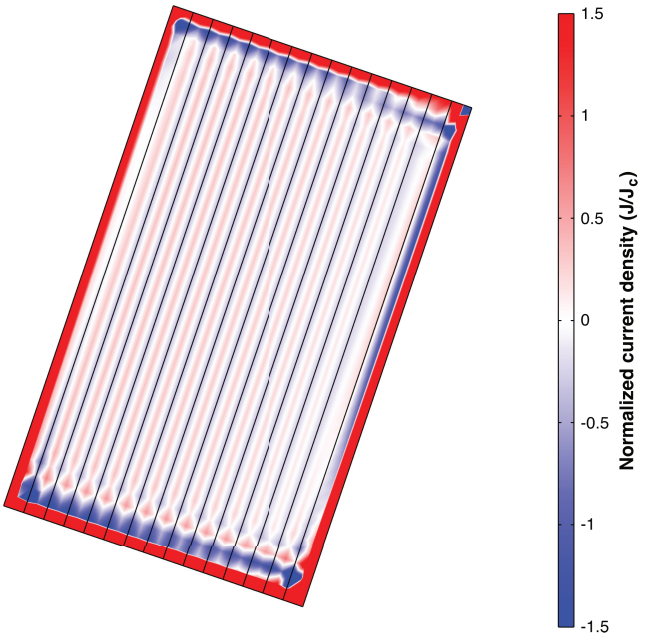

Fig. 14. Current density distribution in the SC coil for the 12-phase machine for a given time instant and normalized by the engineering critical current density. The time instant is handpicked at $0.8375 \cdot \mathrm{T}$ of the steady-state period T, which is one electrical period after the end of the transient period (t_0) of simulation.

It found that using unique phasors or an odd number of phases is an effective winding layout design since only the unique phasors reduce rippling behavior. Moreover, it is proved that the iron losses are further reduced because of the smoother behavior of the magnetic flux densities inside the iron yokes.

The use of symmetric multi-phase FSCWs can further improve the cogging torque without creating space sub-harmonics due to the slot-pole combination giving a higher LCM number. Furthermore, the third symmetry condition is proposed to achieve an optimal design of a multi-phase symmetric-winding SCM. Among the topologies compared, the 13-phase machine stands out by being able to improve the torque density by 34% with respect to the conventional 3-phase machine. The 13-phase topology also has an upper efficiency limit of 99.20%.

The present paper also reveals that the AC hysteresis superconducting losses in a low-frequency machine are strongly affected by the penetration of the magnetic flux lines into the superconductive material, which depends on the tilting angle of the flux lines. Thence, the AC losses can be further reduced by changing the tilting angle of the flux lines by increasing the armature reaction or changing the coil's angular position. However, decreasing the AC losses means that Meisner's effect is increased because there is less penetration of the magnetic flux lines. Therefore, having a strong Meisner's effect in the SCM weakens the machine's mechanical integrity by increasing the pulsating radial forces in the airgap. Thus, twisted or non-planar superconducting armature coils must be designed in 3D with a better superconducting formulation, e.g., the T-A formulation. Moreover, the SC model should have all the wire layers incorporated to optimize the AC

losses and reduce the magnetic field's repulsion, i.e., the so-called Meisner effect. In addition, incorporating iron sheaths, shielding, or other teeth design could improve further the superconductor performance, especially avoiding quenching in the outer areas of the coil due to high magnetic fields.

The findings in this paper advise construction of an AC SCM to measure the fluctuating magnetic behavior due to the Meisner effect and validate the results. In addition, a different PM rotor design could be achieved to improve the magnetic storage capability to enhance the power factor and deal with demagnetization properly. Also, investigate its impact on the increase in the needed PM volume, and on the other hand, explore alternative PM Halbach array-based rotors. Moreover, the design of a power electronic control unit and an algorithm for high-phase order multi-phase symmetric-winding is also part of future work.

APPENDIX A
IRON MATERIAL

The M235-A35 iron material is used in the yoke of the stator and rotor to calculate the iron losses. The B-H curve used in COMSOL is presented in Fig. 15, where the linear extrapolation represents the saturated region where the iron starts working as air. The fitting MATLAB App generates the hysteresis and dynamic losses parameters to calculate the iron losses.

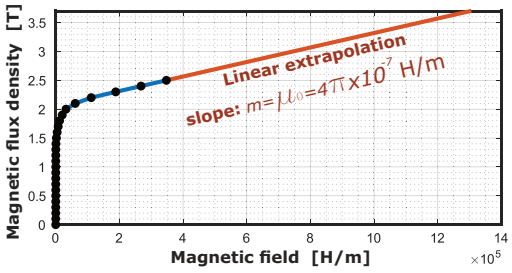

Fig. 15. Curve-fit of the B-H curve of M235-A35 lamination at room temperature.

APPENDIX B
MAXIMAL AND AVERAGE APPLIED PERPENDICULAR MAGNETIC FIELD

The total coverage area of the maximal applied perpendicular magnetic flux density in a range from $1.5\,\mathrm{T}$ to $2.13\,\mathrm{T}$ is depicted in fig. 16. The area coverage is a small fraction in some SC coils, while for others, the area coverage is below this range of magnetic flux. The primary area coverage in the bottom center is around $1.5\,\mathrm{T}$ to $1.7\,\mathrm{T}$. Moreover, in Fig. 16, subfigures (b) and (c), zoom-in pictures are presented. The latter depicts the size of the mesh grid, which gives an insight into the small square on the bottom right of the SC coil. This square represents a calculation area for a boundary condition between the high magnetic field in the air and the SC coil repelling it. In Fig. 12, it is shown that the bottom corners of SC coils have the highest magnetic fields. Therefore, this behavior suggests that a more detailed-level superconductivity formulation must be addressed in future work to avoid potential miss-calculations of the magnetic flux density in certain high-field regions inside the SC coils.

The parallel magnetic fields to the c-axis for each machine are depicted in Fig. 17, where all the coils are integrated to obtain the different values. Moreover, all the machines are simulated for two periods $2{\cdot}T$. Therefore, the 24-phase and 13-phase machines have different periods, $T = \frac{1}{f}$. The operation point is obtained by calculating the mean value of the maximal applied perpendicular magnetic field for all the topologies. It is worth noting that the average perpendicular flux density in the SC material is more than four times low than the peak values in smaller outer regions. A significant portion of the SC material operates at working points even lower than $0.45\,\mathrm{T}$.

Furthermore, the maximal applied field in the c-axis is computed for the inner turns (i.e., neglecting the edges) of the superconducting coils for all the topologies in Fig. 18. The average maximum magnetic flux density within respect to time in this region is $1.77\,\mathrm{T}$, calculated over the second cycle.

REFERENCES

[1] D. L. Asger Bech Abrahamsen and H. Polinder, "Final assessment of superconducting (SC) and Pseudo Direct Drive (PDD) generator performance indicators (PI's). Document information," INNWIND Project, Tech. Rep. Deliverable 3.44, 2017.

[2] E. Union, "SUPRAPOWER: Superconducting, reliable, lightweight, and more powerful offshore wind turbine," This project has received funding from the European Union's Seventh Programme for research, technological development and demonstration under grant agreement number: 308793, Tech. Rep., 2017.

[3] X. Song *et al.*, "Commissioning of the world's first full-scale mw-class superconducting generator on a direct drive wind turbine," *IEEE Transactions on Energy Conversion*, vol. 35, no. 3, pp. 1697–1704, 2020.

[4] I. Marino *et al.*, "Lightweight MgB_2 superconducting 10MW wind generator," *IOP Science : Superconduct. Sci. Tech.*, vol. 29, no. no. 2, pp. 1–11, 2016.

[5] D. Liu, "Increasing the Feasibility of Superconducting Generators for 10 MW Direct-Drive Wind Turbines," Ph.D. dissertation, TU Delft, 2017.

[6] A. Bergen *et al.*, "Design and in-field testing of the world's first rebco rotor for a 3.6 mw wind generator," *Superconduct. Sci. Tech.*, vol. 32, no. 12, p. 125006, 2019.

[7] X. Song *et al.*, "Designing and Basic Experimental Validation of the World's First MW-Class Direct-Drive Superconducting Wind Turbine Generator," *IEEE Trans. Energy Convers.*, vol. 34, no. 4, pp. 2218–2225, 2019.

[8] T. Balachandran, D. Lee, and K. S. Haran, "Optimal design of a fully superconducting machine for 10- mw offshore wind turbines," *Proc. IEEE Int. Electr. Mach. Drives Conf. (IEMDC)*, pp. 1903–1909, 2019.

[9] X. Huang, C. Zhou, K. Zhang, L. Wu, J. Zhang, and W. Cao, "Comparison of electromagnetic performance of scpm wind power generators with different topologies," *IEEE Trans. Appl. Superconduct.*, vol. 29, no. 2, pp. 13–17, 2019.

[10] A. Tessarolo, "Modelling and analysis of multiphase electric machines for high-power applications," Ph.D. dissertation, University of Trieste, 2011.

[11] A. S. Abdel-Khalik, A. Massoud, and S. Ahmed, "Standard three-phase stator frames for multiphase machines of prime-phase order: Optimal selection of slot/pole combination," *IEEE Access*, vol. 7, pp. 78 239–78 259, 2019.

[12] A. S. Abdel-Khalik, S. Mostafa Gadoue, M. I. Masoud, and B. W. Wiliams, "Optimum flux distribution with harmonic injection for a multiphase induction machine using genetic algorithms," *IEEE Trans. Energy Convers.*, vol. 26, no. 2, pp. 501–512, 2011.

[13] G. Yang *et al.*, "Overmodulation strategy for seven-phase induction motors with optimum harmonic voltage injection based on sequential optimization scheme," *IEEE Trans. Power Electron.*, vol. 36, no. 12, pp. 14 039–14 050, 2021.

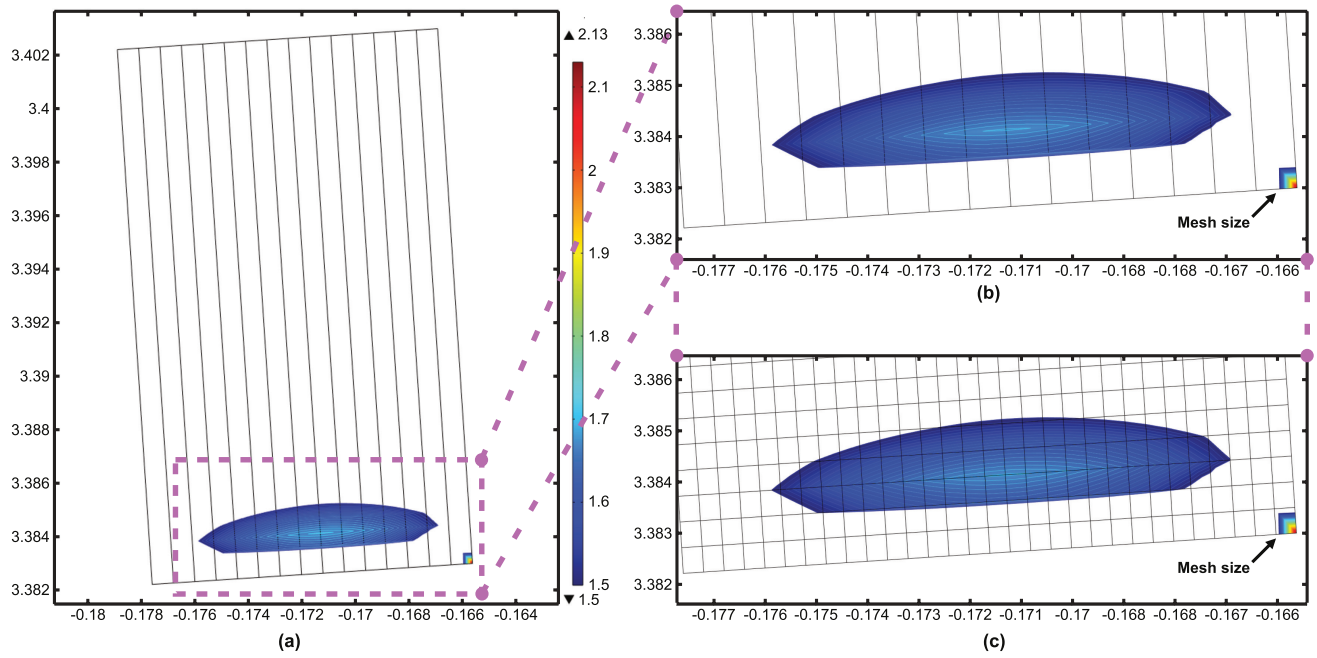

Fig. 16. Maximal applied perpendicular magnetic flux density coverage (B_n). **(a)**: Total SC coil. **(b)**: Zoom into coverage area of SC coil. **(c)**: Zoom into coverage of SC coil with mesh grid.

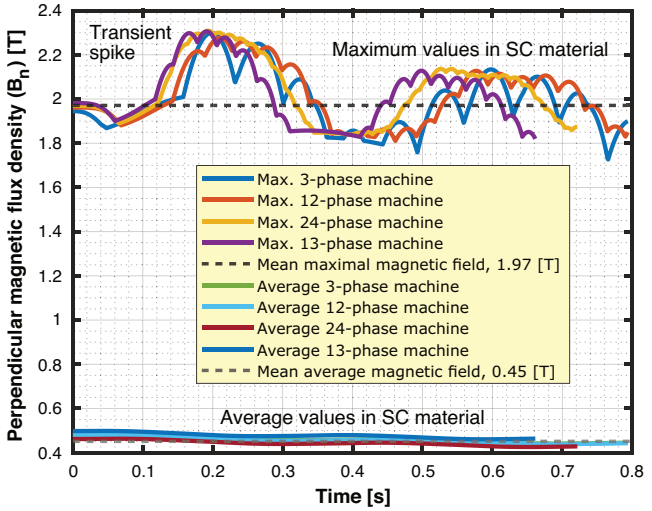

Fig. 17. Maximal and average applied perpendicular magnetic field (B_n), with each machine having slightly different electrical frequency.

pics/maxB_inner_2-eps-converted-to.pdf

Fig. 18. Maximal applied perpendicular magnetic flux density (B_n) of SC coil's inner turns.

[14] Z. Kuang, S. Wu, B. Du, H. Xu, S. Cui, and C. C. Chan, "Thermal Analysis of Fifteen-Phase Permanent Magnet Synchronous Motor under Different Fault Tolerant Operations," *IEEE Access*, vol. 7, pp. 81 466–81 480, 2019.

[15] S. Spas, S. Kowarschik, J. Laumer, M. Wiesinger, and W. Hackmann, "Five-phase ipmsm: Torque density improvement by third harmonic injection," in *Proc. Int. Symp. Power Electron., Electr. Drives, Automat. and Motion (SPEEDAM)*, 2020, pp. 779–786.

[16] V. Tomasov, A. Usoltsev, D. Vertegel, P. Szczepankowski, R. Strzelecki, and N. Poliakov, "Optimized space-vector modulation schemes for five-phase precision low-speed drives with minimizing the stator current ripple," in *Proc. IEEE Int. Conf. Compatib., Power Electron. and Power Eng. (CPE-POWERENG)*, vol. 1, 2020, pp. 279–284.

[17] M. Hossam H. H., A.-R. Youssef, and M. Essam E. M., "Improved perturb and observe MPPT algorithm of multi-phase PMSG based wind energy conversion system," in *Proc. Int. Middle East Power Syst. Conf. (MEPCON)*, 2019, pp. 97–102.

[18] Y. Chen and B. Liu, "Design and analysis of a five-phase fault-tolerant permanent magnet synchronous motor for aerospace starter-generator system," *IEEE Access*, vol. 7, pp. 135 040–135 049, 2019.

[19] C. Chen, H. Zhou, G. Wang, and G. Liu, "Unified Decoupling Vector Control of Five-Phase Permanent-Magnet Motor With Double-Phase Faults," *IEEE Access*, vol. 8, pp. 152 646–152 658, 2020.

[20] H. H. Mousa, A. R. Youssef, and E. E. Mohamed, "Model Predictive Speed Control of Five-Phase PMSG Based Variable Speed Wind Generation System," *2018 20th International Middle East Power Systems Conference, MEPCON 2018 - Proceedings*, pp. 304–309, 2019.

[21] D. J. Tomé Robles, "Superconducting multiphase wind power generator," Master's thesis, NTNU/TU Delft, 2021.

[22] C. H. Lee, "Saturation Harmonics of Polyphase Induction Machines," *Trans. American Inst. Electr. Eng.. Part III: Power App. Syst.*, vol. 80, no. 3, pp. 597–603, 1961.

[23] A. S. Thomas, Z. Q. Zhu, R. L. Owen, G. W. Jewell, and D. Howe, "Multiphase Flux-Switching Permanent-Magnet Brushless Machine for Aerospace Application," *IEEE Trans. Ind. Appl.*, vol. 45, no. 6, pp. 1971–1981, 2009.

[24] V. Kindl, Z. Ferkova, and R. Cermak, "Spatial harmonics in multi-phase induction machine," in *2020 ELEKTRO*, May 2020, pp. 1–4.

[25] V. Kindl, R. Cermak, Z. Ferkova, and B. Skala, "Review of time and space harmonics in multi-phase induction machine," *Energies*, vol. 13, no. 2, 2020.

[26] N. Nibbio, S. Stavrev, and B. Dutoit, "Finite element method simulation of AC loss in HTS tapes with B-dependent E-J power law," *IEEE Trans. Appl. Superconduct.*, vol. 11, no. 1, pp. 2631–2634, 2001.

[27] F. Grilli, E. Pardo, A. Stenvall, D. N. Nguyen, W. Yuan, and F. Gömöry, "Computation of losses in hts under the action of varying magnetic fields and currents," *IEEE Trans. Appl. Superconduct.*, vol. 24, no. 1, pp. 78–110, 2014.

[28] J. Pyrhönen, T. Jokinen, and V. Hrabovcov, *Design of Rotating Electrical Machines*. Chichester, UK: John Wiley & Sons, Ltd, dec 2008.

[29] D. Liu, X. Song, and X. Wang, "Design challenges of direct-drive permanent magnet superconducting wind turbine generators," in *Proc. Int. Conf. Electr. Mach. (ICEM)*, vol. 1, 2020, pp. 640–646.

[30] D. Liu *et al.*, "Short-circuit characteristics of superconducting permanent magnet generators for 10 MW wind turbines," *IEEE Trans. Appl. Superconduct.*, vol. 31, no. 5, pp. 4–8, 2021.

[31] E. Snider *et al.*, "Room-temperature superconductivity in a carbonaceous sulfur hydride," *Nature*, vol. 586, no. 7829, pp. 373–377, 2020.

[32] M. D. Sumption, F. Wan, M. Rindfleisch, and M. Tomsic, "Ac loss of superconducting materials-refined loss estimates of mgb2 wires for superconducting motors and generators," *AIAA Propulsion and Energy Forum and Exposition, 2019*, no. August, 2019.

[33] F. Wan, M. D. Sumption, M. A. Rindfleisch, M. J. Tomsic, and E. W. Collings, "Architecture and Transport Properties of Multifilamentary MgB2 Strands for MRI and Low AC Loss Applications," *IEEE Transactions on Applied Superconductivity*, vol. 27, no. 4, pp. 1–5, 2017.

[34] K. Tsuchiya *et al.*, "Critical current measurement of commercial REBCO conductors at 4.2 K," *Cryogenics*, vol. 85, pp. 1–7, jul 2017.

[35] R. Brambilla, F. Grilli, L. Martini, M. Bocchi, and G. Angeli, "A finite element method framework for modeling rotating machines with superconducting windings," *arXiv*, vol. 28, no. 5, 2017.

[36] F. Inanir and R. Terzioglu, "AC loss evaluation of a superconducting pancake coil with coated conductors using an extended av formulation," *Physica C: Superconduct. and its Appl.*, p. 1353910, 2021.

[37] M. Komiya *et al.*, "Design study of 10 MW REBCO fully superconducting synchronous generator for electric aircraft," *IEEE Trans. Appl. Superconduct.*, vol. 29, no. 5, pp. 1–6, 2019.

[38] S. Miura, M. Iwakuma, and T. Izumi, "Lightweight Design of Tens-MW Fully-Superconducting Wind Turbine Generators with High-Performance REBa2Cu3Oy Wires," *IEEE Trans. Appl. Superconduct.*, vol. 30, no. 4, pp. 3–8, 2020.

[39] M. Komiya *et al.*, "Conceptual Design and Numerical Analysis of 10 MW Fully Superconducting Synchronous Generators Installed with a Novel Casing Structure," *IEEE Trans. Appl. Superconduct.*, vol. 30, no. 4, 2020.

[40] N. Nibbio, S. Stavrev, and B. Dutoit, "Finite element method simulation of AC loss in HTS tapes with B-dependent E-J power law," *IEEE Trans. Appl. Superconduct.*, vol. 11, no. 1, pp. 2631–2634, 2001.

[41] E. Gaertner *et al.*, "Definition of the IEA 15-Megawatt Offshore Reference Wind Turbine," National Renewable Energy Laboratory NREL, Tech. Rep., 2020.

[42] S. Vaschetto, A. Tenconi, and G. Bramerdorfer, "Sizing procedure of surface mounted PM machines for fast analytical evaluations," *Proc. IEEE Int. Electr. Mach. Drives Conf. (IEMDC)*, vol. 63, 2017.

[43] Z. Q. Zhu and D. Howe, "Influence of design parameters on cogging torque in permanent magnet machines," *IEEE Trans. Energy Convers.*, vol. 15, no. 4, pp. 407–412, 2000.

[44] D. M. Ionel, M. Popescu, M. I. McGilp, T. J. E. Miller, S. J. Dellinger, and R. J. Heideman, "Computation of core losses in electrical machines using improved models for laminated steel," *IEEE Trans. Ind. Appl.*, vol. 43, no. 6, pp. 1554–1564, Nov 2007.

[45] T. H. Akinaga, T. Staudt, W. Hoffmann, C. E. Soares, A. A. de Espíndola, and J. P. A. Bastos, "A comparative investigation of iron loss models for electrical machine design using FEA and experimental validation," in *Proc. Int. Conf. Electr. Mach. (ICEM)*, 2018, pp. 461–466.

[46] D. M. Ionel, M. Popescu, M. I. McGilp, T. J. E. Miller, S. J. Dellinger, and R. J. Heideman, "Computation of core losses in electrical machines using improved models for laminated steel," *IEEE Trans. Ind. Appl.*, vol. 43, no. 6, pp. 1554–1564, 2007.

[47] K. Wang and H. Lin, "A novel 24-slot/10-pole dual three-phase fractional-slot overlapped winding for low non-working space harmonics and stator modularization," *IEEE Access*, vol. 8, pp. 85 490–85 503, 2020.

[48] M. Farshadnia, *Advanced Theory of Fractional-Slot Concentrated-Wound Permanent Magnet Synchronous Machines*, 1st ed. Springer Singapore, 2018.

[49] J. K. Nøland, C. M. Hartmann, and R. Mellerud, "Next-generation cryo-electric hydrogen-powered aviation: A disruptive superconducting propulsion system cooled by onboard cryogenic fuels," *IEEE Ind. Electron. Mag.*, pp. 2–11, 2022.

[50] S. Ozaki, H. Hirai, M. Hirokawa, and H. Kobayashi, "Development of 10 kw turbo-brayton refrigerator for hts power applications," in *IOP Conf. Ser.: Materials Science and Eng.*, vol. 502, no. 1. IOP Publishing, 2019, p. 012008.

[51] H.-J. Sung, M. Park, B.-S. Go, and I.-K. Yu, "A study on the required performance of a 2g hts wire for hts wind power generators," *Superconduct. Sci. Tech.*, vol. 29, no. 5, p. 054001, 2016.

[52] C. R. Vargas-Llanos, S. Lengsfeld, M. Noe, T. Arndt, and F. Grilli, "Influence of coil position on ac losses of stator superconducting windings of a synchronous machine for a 10 MW wind turbine," *IEEE Trans. Appl. Superconduct.*, vol. 31, no. 7, pp. 1–9, 2021.

[53] A. Musso, M. Breschi, P. L. Ribani, and F. Grilli, "Analysis of AC Loss Contributions from Different Layers of HTS Tapes Using the A-V Formulation Model," *IEEE Trans. Appl. Superconduct.*, vol. 31, no. 2, 2021.

[54] H. Sasa *et al.*, "Thermal-Electromagnetic Coupled Analysis Considering AC Losses in REBCO Windings at 65 K of 10 MW Fully-Superconducting Synchronous Generators for Electric Aircraft," *IEEE Trans. Appl. Superconduct.*, vol. 32, no. 6, pp. 1–1, 2022.

[55] H. Sasa, S. Miura, M. Iwakuma, T. Izumi, T. Machi, and A. Ibi, "Estimation Method for AC Loss of Perpendicularly Stacked REBa2Cu3O Superconducting Tapes under Magnetic Field," *Physica C: Superconduct. and its Appl.*, vol. 580, no. November 2020, p. 1353801, jan 2021.

[56] A. Tessarolo, "A Quadratic-Programming Approach to the Design Optimization of Fractional-Slot Concentrated Windings for Surface Permanent-Magnet Machines," *IEEE Trans. Energy Convers.*, vol. 33, no. 1, pp. 442–452, 2018.

[57] A. Tessarolo, C. Ciriani, M. Bortolozzi, M. Mezzarobba, and N. Barbini, "Investigation into Multi-Layer Fractional-Slot Concentrated Windings with Unconventional Slot-Pole Combinations," *IEEE Trans. Energy Convers.*, vol. 34, no. 4, pp. 1985–1996, 2019.

[58] A. Tessarolo, C. Ciriani, N. Elloumi, and M. Mezzarobba, "Potentials and limits of three-phase fractional-slot concentrated winding optimization," *Proceedings - 2021 IEEE Workshop on Electrical Machines Design, Control and Diagnosis, WEMDCD 2021*, pp. 143–148, 2021.

[59] M. J. Duran, E. Levi, and F. Barrero, "Multiphase Electric Drives: Introduction," in *Wiley Encyclopedia of Electrical and Electronics Engineering*. Hoboken, NJ, USA: John Wiley & Sons, Inc., nov 2017, no. i, pp. 1–26.

[60] J. Huang, M. Kang, J. Q. Yang, H. B. Jiang, and D. Liu, "Multiphase machine theory and its applications," *Proc. 11th Int. Conf. Electr. Mach. Syst. (ICEMS)*, pp. 1–7, 2008.

[61] W. Kong, J. Huang, R. Qu, M. Kang, and J. Yang, "Nonsinusoidal Power Supply Analysis for Concentrated-Full-Pitch-Winding Multiphase Induction Motor," *IEEE Trans. Ind. Electron.*, vol. 63, no. 1, pp. 574–582, jan 2016.

[62] W. Kong, R. Qu, M. Kang, J. Huang, and L. Jing, "Air-Gap and Yoke Flux Density Optimization for Multiphase Induction Motor Based on Novel Harmonic Current Injection Method," *IEEE Trans. Ind. Appl.*, vol. 53, no. 3, pp. 2140–2148, may 2017.

[63] D. T. Vu, N. K. Nguyen, E. Semail, and H. Wu, "Adaline-Based Control Schemes for Non-Sinusoidal Multiphase Drives–Part I: Torque Optimization for Healthy Mode," *Energies*, vol. 14, no. 24, p. 8302, dec 2021.

[64] ——, "Adaline-Based Control Schemes for Non-Sinusoidal Multiphase Drives—Part II: Torque Optimization for Faulty Mode," *Energies*, vol. 15, no. 1, p. 249, dec 2021.

[65] A. Trentin *et al.*, "Research and Realization of High-Power Medium-Voltage Active Rectifier Concepts for Future Hybrid-Electric Aircraft Generation," *IEEE Trans. Ind. Electron.*, vol. 68, no. 12, pp. 11 684–11 695, 2021.

Dany Josué Tomé Robles (M'22) was born in Tegucigalpa, Honduras, in 1992. He received two Bachelor's degrees in Physics and Electrical Engineering from the National Autonomous University of Honduras (UNAH). In August 2021, he finished a joint MSc degree from the European Wind Energy Master (EWEM) program at Delft University of Technology (TU Delft), the Netherlands, and the Norwegian University of Science and Technology (NTNU), Norway. Currently, he is a PhD candidate at the University of South-Eastern Norway (USN) in the SysOpt project. His research interests include AC superconducting coils, Multi-Phase machines, the design of compact machines, electromagnetics, Power System Analysis and Dynamics.

Robert Nilssen received the M.Sc. and Ph.D. degrees from the Norwegian University of Science and Technology (NTNU), Trondheim, Norway, in 1983 and 1989, respectively, specializing in finite-element analysis (FEA) and electrical machines (EMs). He is currently a Full Professor with the Department of Electrical Power Engineering (IEL), NTNU. His research interests include design, optimization, and modeling of industrial EMs for various applications.

Jonas Kristiansen Nøland (S'14-M'17-SM'22) was born in Drammen, Norway, in 1988. He received the Ph.D. degree in engineering physics from Uppsala University, Uppsala, Sweden, in 2017. Since 2018, he has been an Associate Professor with the Norwegian University of Science and Technology. His main research interests are enabling technologies for electrification in the energy generation and transportation sectors. Dr. Nøland serves as an Associate Editor for the IEEE TRANSACTIONS ON ENERGY CONVERSION and the IEEE TRANSACTIONS ON INDUSTRIAL ELECTRONICS.